SEMIANNUAL REPORT FOR

Grant No. NAG 1-500

SEMICONDUCTOR SUPERLATTICE PHOTODETECTORS

July 1, 1985 to December 31, 1985

Submitted to

Dr. Ivan Clark

National Aeronautics and Space Administration
Langley Research Center, Mail Stop 473
Hampton, VA 23665

Prepared by

S. L. Chuang
Department of Electrical and Computer Engineering
University of Illinois
Urbana, IL 61801

K. Hess, J. J. Coleman and J. P. Leburton
Department of Electrical and Computer Engineering
and Coordinated Science Laboratory
University of Illinois
Urbana, IL 61801

SEMIANNUAL REPORT FOR

Grant No. NAG 1-500

SEMICONDUCTOR SUPERLATTICE PHOTODETECTORS

July 1, 1985 to December 31, 1985

Submitted to

Dr. Ivan Clark

National Aeronautics and Space Administration
Langley Research Center, Mail Stop 473
Hampton, VA 23665

Prepared by

S. L. Chuang
Department of Electrical and Computer Engineering
University of Illinois
Urbana, IL 61801

K. Hess, J. J. Coleman and J. P. Leburton
Department of Electrical and Computer Engineering
and Coordinated Science Laboratory
University of Illinois
Urbana, IL 61801

TABLE OF CONTENTS

I. INTRODUCTION

The research grant NAG 1-500 entitled "Semiconductor Superlattice Photodetectors" was awarded to the University of Illinois at Urbana-Champaign by National Aeronautics and Space Administration-Langley Research Center on June 27, 1984. The grant was continued on July 1, 1985. Dr. Ivan Clark is the Technical Officer, and Mr. John F. Royall is the Grants Officer.

This report is the third semiannual report.

1. Period:

   July 1, 1985 to December 31, 1985

2. Reporting Date:

   January 10, 1986.

3. Technical Personnel:

   S. L. Chuang — Assistant Professor of Electrical and Computer Engineering

   J. J. Coleman — Professor of Electrical and Computer Engineering

   K. Hess — Professor of Electrical and Computer Engineering and Research Professor of Coordinated Science Laboratory

   J. P. Leburton — Assistant Professor of Electrical and Computer Engineering and Research Assistant Professor of Coordinated Science Laboratory

   Two research assistants

II. TECHNICAL PROGRESS

During the past half-year period, we continued the work on the new superlattice photomultiplier with the following effects investigated. The detailed analysis is included in the Appendix of this report. Here we give a brief description.

(1) The effect of multiple subbands

Since the quantum-well regions may contain several subbands, each of which may be occupied by electrons depending on the doping concentrations, it is important to include the multi-subbands in calculating the impact ionization rate. The electrons occupying the higher subbands require a smaller amount of energy to get out of the quantum well; thus, those higher level subband electrons contribute significantly to the impact ionization rate. The results of the multiple subbands have been calculated. (Please see page 17 of the Appendix.)

(2) The nonparabolicity effect of the band structure

Since the electron energies involved are of the order of 0.3 eV or higher, the nonparabolic band structure may be important. That is, the effective mass of the electrons may be larger than the effective mass of the electrons at the band edge of the Γ valley. Thus, an averaging procedure has been used to find an average effective mass of the electrons that takes into account the nonparabolicity effect. (Page 26 of the Appendix)

(3) The effect of the quantum-well size

The quantum-well size determines the energy levels and the Fermi level for a given doping concentration. Changing the well width will change the impact ionization rate. It is found that for the same doping concentration in the quantum wells, the well with a thicker dimension will have a larger ionization rate because there are more electrons available for ionization in a thicker well.

(4) The effect of the band-edge discontinuity

The band-edge discontinuity affects the threshold energy for impact ionization. A smaller band edge discontinuity will give a larger impact ionization rate because the threshold energy required for impact ionization is smaller. (Page 18 of the Appendix)

(5) The effect of doping

The doping concentration decides the number of electrons available for impact ionization. Increasing the doping concentrations will increase the impact ionization rate. The results of various dopings are shown in Figure 7 of the Appendix and discussed on page 19 of the Appendix.

III. FUTURE WORK

Recently, Capasso at AT&T Bell Laboratories has independently performed experiments on similar types of structures and obtained encouraging evidence for impact ionization of the kind discussed in this research. These experiments may call for an extension of our theory to include effects such as the tunneling-supported impact ionization and the impact ionization from deep impurity centers. We shall investigate these effects and others such as the thermionic emissions. These studies will certainly provide more insight into the physics of the superlattice photodetectors.

IV. PUBLICATIONS

The following manuscripts submitted for publication were supported either fully or partially by this Grant. The support by this Grant has been acknowledged in these manuscripts.

1. S. L. Chuang and K. Hess, "Impact ionization across the conduction band edge discontinuity of quantum-well heterostructures", J. Appl. Phys., accepted for publication.

2. S. L. Chuang, "Lateral shift of an optical beam due to leaky surface plasmon excitations", J. Opt. Soc. Am., accepted for publication.

3. S. L. Chuang, "Anisotropic wave propagation in a superlattice waveguide," submitted for publication.

V. TRAVEL

S. L. Chuang attended the 1985 International Electron Devices Meeting at Washington D. C., Dec. 1-4, 1985. He also attended a short course on "Digital III-V Device and Circuit Technology" during that meeting.

APPENDIX

"Impact Ionization Across the Conduction Band Edge Discontinuity of Quantum-Well Heterostructures" By S. L. Chuang and K. Hess.

IMPACT IONIZATION ACROSS THE CONDUCTION BAND EDGE DISCONTINUITY OF QUANTUM-WELL HETEROSTRUCTURES

S. L. Chuang

Department of Electrical and Computer Engineering
University of Illinois at Urbana-Champaign, Urbana, IL 61801

K. Hess

Department of Electrical and Computer Engineering
and Coordinated Science Laboratory
University of Illinois at Urbana-Champaign, Urbana, IL 61801

ABSTRACT

Impact ionization across the band edge discontinuity of quantum-well heterostructures is studied theoretically. We consider a heterolayer structure of alternating $A\ell_x Ga_{1-x}As$ and GaAs layers where the GaAs layers are heavily doped with donors. Thus a large number of electrons is confined to the quantum-well region. Incident electrons are heated up by applied electric fields and collide with the electrons confined in the well regions. Both the ionization rate as a function of the incident energy, and average ionization rates are computed. Device applications of such multiple quantum well structures and the possibility of a complete analog to the conventional photomultiplier are discussed.

1. INTRODUCTION

Novel types of photodetectors using superlattice structures have been proposed recently[1-10]. These include the enhancement of impact ionization in a superlattice for avalanche photodiodes,[1-6] an infrared detector using free carrier absorption in a heavily doped quantum-well structure,[7] a photodetector using the transient displacement current effect in a sawtooth superlattice,[8] strained-layer superlattice photodetectors[9,10] and doping (n-i-p-i) photodetectors.[11,12] The operational principles of all these new devices are very interesting and additional studies are needed to characterize these photodetectors completely.

In this paper, we consider a heterolayer structure which consists of alternating $A\ell_xGa_{1-x}As$ and GaAs layers where the GaAs layers are heavily doped with donors (Figure 1). The donor are electrons confined mostly to the quantum wells. Incident electrons (which for example can be generated optically) are accelerated by the external field and collide with the electrons confined in the wells as shown in Figure 1. This results in impact ionization of some of the electrons bound in the quantum wells. The wave functions for the incident electrons (three-dimensional) and the confined electrons (quasi-two dimensional) are used to calculate the electron-electron interaction due to the Coulomb force with screening effects taken into account. The quantum mechanical transition rate for a system involving an initial state of one free electron above the well and one bound electron in the well and a final state of both electrons free is calculated using the Golden rule. The process is schematically displayed in Figure 2. The electron-electron interaction in the momentum space is illustrated in Figure 3 and will be explained in the next section. The average ionization rate over the momentum (energy) distribution of all the incident hot electrons

is then calculated. Potential device applications are discussed in a final section.

Our formulation for the impact ionization for the quantum-well structure is similar to the inverse Auger effect in bulk semiconductors[13-17] or in a quantum-well heterostructure.[18-19] The new feature is that we are interested in impact ionization across the conduction band edge discontinuity while previous studies are considering transitions across the energy band gap. Thus, the threshold energy for impact ionization is smaller (of the order of conduction band edge discontinuity) than that of the interband process. The required bias voltage may be smaller since a smaller electric field than that of the conventional avalanche photodiode is needed.

2. ANALYTICAL CONSIDERATIONS

In this section, we present the detailed formulation of the impact ionization of electrons across the conduction band edge discontinuity in a heterolayer structure. First the transition rate due to the electron-electron interaction is derived, then we discuss the energy distributions of the electrons confined in the quantum-well region and the incident hot electrons. Third we present the impact ionization rate and its numerical evaluation.

2.1. Transition Rate

Consider an incident free electron interacting with a bound electron in a quantum well; the total average transition rate per unit volume P_{tr} is given by[19,20]

$$P_{tr} = \frac{1}{V} \sum_{\vec{k}_1} \sum_{\vec{k}_2} \sum_{\vec{k}_1'} \sum_{\vec{k}_2'} P_{\vec{k}_1 \vec{k}_2}^{\vec{k}_1' \vec{k}_2'} f(\vec{k}_1)\, f(\vec{k}_2)\, [1 - f(\vec{k}_1')][1 - f(\vec{k}_2')] \tag{1}$$

where f is the Fermi distribution and $P_{\vec{k}_1 \vec{k}_2}^{\vec{k}_1' \vec{k}_2'}$ is the quantum mechanical transition rate (per unit time) between the initial state of electron 1 in state $\vec{k}_1$, electron 2 in state $\vec{k}_2'$ and the final state of electron 1 in state $\vec{k}_1'$ and electron 2 in state $\vec{k}_2'$ (Figure 2) due to the electron-electron interaction:

$$P_{\vec{k}_1 \vec{k}_2}^{\vec{k}_1' \vec{k}_2'} = \frac{2\pi}{\hbar} |\langle 12 | H_s | 1'2' \rangle|^2 \, \delta(E_1 + E_2 - E_1' - E_2') \quad . \tag{2}$$

The square of the matrix element $|\langle 12 | H_s | 1'2' \rangle|^2$ is given by

$$|\langle 12 | H_s | 1'2' \rangle|^2 = 4 \left| \int \psi_{\vec{k}_1}^{*}(\vec{r}_1)\, \psi_{\vec{k}_2}^{*}(\vec{r}_2)\, \frac{e^2 \exp(-q|\vec{r}_1 - \vec{r}_2|)}{4\pi\, \varepsilon\, |\vec{r}_1 - \vec{r}_2|}\, \psi_{\vec{k}_1'}(\vec{r}_1)\, \psi_{\vec{k}_2'}(\vec{r}_2)\, d\vec{r}_1 d\vec{r}_2 \right|^2 \tag{3}$$

for the interaction by a screened Coulomb potential. Here q is the screening parameter which is discussed in Appendix A. We have neglected the difference in the dielectric constants of the two materials which is a good approximation for AlGaAs-GaAs. The factor of 4 in Equation (3) takes account of effects of the exchange and preservation of the spin[14,15], considering the integrations over $\vec{k}_1'$ and $\vec{k}_2'$, and

$$\langle \vec{r}_1 \vec{r}_2 | 12 \rangle \equiv \psi_{\vec{k}_1}(\vec{r}_1)\, \psi_{\vec{k}_2}(\vec{r}_2)$$

$$= \frac{\exp(i\vec{k}_1 \cdot \vec{r}_1)}{\sqrt{V}} \cdot \sqrt{\frac{2}{AL_{zn}}} \exp(i\vec{k}_{2t} \cdot \vec{r}_{2t}) \sin \frac{n\pi}{L_{zn}} z_2 \qquad (4)$$

$$\langle \vec{r}_1 \vec{r}_2 | 1'2' \rangle \equiv \psi_{\vec{k}_1'}(\vec{r}_1)\, \psi_{\vec{k}_2'}(\vec{r}_2)$$

$$= \frac{\exp(i\vec{k}_1' \cdot \vec{r}_1)}{\sqrt{V}} \frac{\exp(i\vec{k}_2' \cdot \vec{r}_2)}{\sqrt{V}} \qquad (5)$$

where $\vec{k}_1$, $\vec{k}_1'$, $\vec{k}_2'$, $\vec{r}_1$, $\vec{r}_2$ are the general three-dimensional vectors and $\vec{k}_{2t}$, $\vec{r}_{2t}$ are two-dimensional vectors in the quantum well interface planes. The Bloch functions associated with Equations (4) and (5) have been ignored since the overlap integral is assumed to be one for states in the conduction band. The effective quantum well width L_{zn} is defined such that

$$E_{Qn} = \frac{\hbar^2}{2m^*} \left(\frac{n\pi}{L_{zn}}\right)^2 \qquad (6)$$

where E_{Qn} is the energy level of the nth subband, which is calculated numerically taking into account the finite barrier height ΔE_c, i.e., the conduction band edge discontinuity (See Appendix B). For convenience, we further define:

$$\vec{k}_{2n}^{\pm} = \vec{k}_{2t} \pm \hat{z}\frac{n\pi}{L_z} = \hat{x}k_x + \hat{y}k_y \pm \hat{z}\frac{n\pi}{L_{zn}} \tag{7}$$

$$\vec{r}_2 = \vec{r}_{2t} + \hat{z}z_2 = \hat{x}x_2 + \hat{y}y_2 + \hat{z}z_2 \quad , \tag{8}$$

and replace the summations $\sum_{\vec{k}}$ by integrations. One then obtains

$$|\langle 12|H_s|1'2'\rangle|^2 \simeq \left(\frac{e^2}{\epsilon V}\right)^2 \left(\frac{2L_{zn}}{L}\right) \frac{1}{[|\vec{k}_1 - \vec{k}_1'|^2 + q^2]^2} [\delta_{\vec{k}_1+\vec{k}_2^+,\vec{k}_1'+\vec{k}_2'} + \delta_{\vec{k}_1+\vec{k}_2^-,\vec{k}_1'+\vec{k}_2'}] \tag{9}$$

and

$$P_{tr} \simeq \frac{e^4}{\epsilon^2}\frac{4\pi}{\hbar}\left(\frac{L_{zn}}{L}\right)^2 \int \frac{d\vec{k}_1}{(2\pi)^3} f(\vec{k}_1) \int \frac{d\vec{k}_{2t}}{(2\pi)^2 L_{zn}} f(\vec{k}_{2t})[S(\vec{k}_1,\vec{k}_{2n}^+) + S(\vec{k}_1,\vec{k}_{2n}^-)] \tag{10}$$

Here we have used the fact that $f(\vec{k}_1')$ and $f(\vec{k}_2') \ll 1$, also $f(\vec{k}_{2t}) = f(\vec{k}_2^+) = f(\vec{k}_2^-)$ (which will be discussed later) and

$$S(\vec{k}_1,\vec{k}_{2n}^{\pm}) \equiv \int_{\substack{k_{1z}' \geq k_{th}' \\ k_{2z}' \geq k_{th}'}} \frac{d\vec{k}_1'}{(2\pi)^3} \frac{\delta(E_1 + E_2 - E_1' - E_2')}{[|\vec{k}_1 - \vec{k}_1'|^2 + q^2]^2}\Bigg|_{\vec{k}_2'=\vec{k}_1+\vec{k}_{2n}^{\pm}-\vec{k}_1'} . \tag{11}$$

The lower limit in the integration for $\vec{k}_1'$ is due to the fact that both k_{1z}' and k_{2z}' need to be larger than a certain threshold k_{th}' in order to get both electrons 1' and 2' out of the quantum well. The condition $k_{2z}' \geq k_{th}'$ imposes another condition on k_{1z}' because of the relation $k_{2z}' = k_{1z} \pm \frac{n\pi}{L_{zn}} - k_{1z}' \geq k_{th}'$. One finally obtains

$$k'_{th} \leq k'_{1z} \leq k_{1z} \pm \frac{n\pi}{L_{zn}} - k'_{th} \quad . \tag{12}$$

One notes that the above condition for k'_{1z} also holds for k'_{2z} obviously.

An upper bound of the integral of Equation (11) without the constraints on k'_{1z} and k'_{2z} has been obtained analytically for a parabolic band structure[21].

$$S_u(\vec{k}_1, \vec{k}^{\pm}_{2n}) \equiv \int_{\substack{all \\ \vec{k}'_1}} \frac{d\vec{k}'_1}{(2\pi)^3} \frac{\delta(E_1 + E_2 - E'_1 - E'_2)}{[|\vec{k}_1 - \vec{k}'_1|^2 + q^2]^2} \Bigg|_{\vec{k}'_2 = \vec{k}_1 + \vec{k}^{\pm}_{2n} - \vec{k}'_1}$$

$$= \frac{m^*}{8\pi^2 \hbar^2 q^2} \frac{|\vec{k}_1 - \vec{k}^{\pm}_{2n}|}{|\vec{k}_1 - \vec{k}^{\pm}_{2n}|^2 + q^2} \quad . \tag{13}$$

The geometry pertinent to the evaluation of $S(\vec{k}_1, \vec{k}_2)$ and its upper bound $S_u(\vec{k}_1, \vec{k}_2)$ is shown in Figure 3, for $\vec{k}_2 \equiv \vec{k}^{+}_{2n} = \vec{k}_{2t} + \hat{z}\frac{n\pi}{L_{zn}}$ (n=1). Due to energy and momentum-conservations, the four vectors $\vec{k}_1$, $\vec{k}_2$, $\vec{k}'_1$ and $\vec{k}'_2$ lie on a spherical surface assuming that the E-$\vec{k}$ relations are parabolic, for all four vectors[22]. Due to the above mentioned constraints, on both k'_{1z} and k'_{2z}, the $S(\vec{k}_1, \vec{k}_2)$ integral will be over the unshaded spherical surface in Figure 3 for which $k'_{th} \leq k'_{1z} \leq k_{1z} + \frac{\pi}{L_{z1}} - k'_{th}$, while the integral for $S_u(\vec{k}_1, \vec{k}_2)$ is over the whole spherical surface. The latter integration can be peformed analytically by a coordinate transformation to the polar axis $\vec{k}_1 - \vec{k}_2$, and results in Equation (13).

2.2. Electron Distribution Function $f(\vec{k}_2)$ in the Quantum-Well Region

The electron distribution function in the quantum-well region $f(\vec{k}^{\pm}_2)$ or $f(\vec{k}_{2t})$ is taken as

$$f(\vec{k}_{2t}) = \begin{cases} 1 & \text{if } 0 \leq k_{2t} \leq K^{(n)}_{2t} \\ 0 & \text{otherwise} \end{cases} \tag{14}$$

where

$$K_{2t}^{(n)} = \sqrt{\frac{2m^*}{\hbar^2} E_F - \left(\frac{n\pi}{L_{zn}}\right)^2} \tag{15}$$

is the maximum of k_{2t} for electrons in the n-th subband.

The electron concentration is given by

$$n = \int_{E_{Q1}}^{\infty} f(E)\, g(E)\, dE$$

$$= \sum_n \frac{m^*}{\pi\hbar^2 L_z} k_B T \ln[1 + e^{(E_F - E_{Qn})/k_B T}] \tag{16}$$

where E_{Qn} is the n-th quantized energy level of electron 2 as given in Equation (6). Defining a characteristic concentration n_c,

$$n_c \equiv \frac{m^* k_B T}{\pi\hbar^2 L_z} . \tag{17}$$

We have for $E_F - E_{Qn} >> k_B T$,

$$\frac{n}{n_c} = \sum_{\substack{\text{occupied} \\ \text{subbands } n}} (E_F - E_{Qn})/k_B T . \tag{18}$$

From $n \approx N_D$ and the above relation or (16), we obtain E_F, and thus $K_{2t}^{(n)}$.

2.3. Electron Distribution Function $f(\vec{k}_1)$ for the Incident Hot Electrons

We assume that the incident hot electrons in the $Al_xGa_{1-x}As$ region (region a) is Maxwellian in shape, i.e., the spherically symmetrical part is given by the expression:

$$f(\vec{k}_0) = 4n_0 \left(\frac{\pi\hbar^2}{2m_a^* k_B T_e}\right)^{3/2} e^{-E_0(\vec{k}_0)/k_B T_e} \tag{19}$$

with an electron temperature T_e, where m_a^* is the effective mass of the electron in the conduction band in the $Al_xGa_{1-x}As$ region and the index 0 characterizes

the electrons in this region. Since the energy

$$E_0 = \frac{\hbar^2}{2m_a^*}(k_{0x}^2 + k_{0y}^2 + k_{0z}^2) \tag{20}$$

is measured from the conduction band edge in the $A\ell_xGa_{1-x}As$ region, and

$$\vec{k}_0 = k_{0x}\hat{x} + k_{0y}\hat{y} + k_{0z}\hat{z} \quad , \tag{21}$$

the energy E_1 and $\vec{k}_1$ vector in the GaAs region (region b) are related to E_0 and $\vec{k}_0$ by the equations

$$k_{1x} = k_{0x} \tag{22}$$

$$k_{1y} = k_{0y} \tag{23}$$

$$\frac{\hbar^2}{2m_a^*} k_0^2 + \Delta E_c = \frac{\hbar^2}{2m_b^*} k_1^2 \tag{24}$$

where m_b^* is the average effective mass of electrons in the Γ-valley of the GaAs region. (We use the average effective mass m_b^* to include the nonparabolicity effect. The effective mass m^* used in the previous equations is replaced by m_b^* in the computations. See Appendix C). Instead of integrating over $d\vec{k}_1$, we integrate over $d\vec{k}_0$,

$$\int \frac{d\vec{k}_1}{(2\pi)^3} f(\vec{k}_1) \rightarrow \int \frac{d\vec{k}_0}{(2\pi)^3} f_0(\vec{k}_0) \quad .$$

2.4. Average Impact Ionization Rate

The average ionization rate $\langle\frac{1}{\tau}\rangle$ is defined as the total transition rate per incident electron and therefore:

$$\left\langle \frac{1}{\tau} \right\rangle = \frac{P_{tr}}{n_0}$$

$$= \int \frac{d\vec{k}_0}{(2\pi)^3} 4\left(\frac{\pi\hbar^2}{2m_a^* k_B T_e}\right)^{3/2} \exp\left[-\frac{\hbar^2}{2m_a^* k_B T_e}\left(k_{0x}^2+k_{0y}^2+k_{0z}^2\right)\right] \frac{1}{\tau(E_0)}$$

$$\simeq \int \frac{dk_{0z}}{2\pi} \left(\frac{\pi\hbar^2}{2m_a^* k_B T_e}\right)^{1/2} \exp\left[-\frac{\hbar^2 k_{0z}^2}{2m_a^* k_B T_e}\right] \frac{1}{\tau(E_{0z})} \tag{25}$$

where

$$\frac{1}{\tau(E_{0z})} = \frac{e^4}{\varepsilon^2}\frac{4\pi}{\hbar^2}\left(\frac{L_{zn}}{L}\right)^2 \int \frac{d\vec{k}_{2t}}{(2\pi)^2 L_{zn}} f(\vec{k}_{2t})\left[S(\vec{k}_1,\vec{k}_{2n}^{+}) + S(\vec{k}_1,\vec{k}_{2n}^{-})\right] \tag{26}$$

which is the ionization rate for an incident hot electron with the energy

$$E_0 = E_{0z} = \frac{\hbar^2}{2m_a^*} k_{0z}^2 \tag{27}$$

and

$$k_{0x} = k_{0y} = 0 \tag{28}$$

Since the integrand in (25) is sharply peaked near $k_{0x} = k_{0y} \simeq 0$, we have used the approximations

$$\frac{1}{\tau(E_0)} \simeq \frac{1}{\tau(E_0)}\Bigg|_{\substack{k_{0x}=0 \\ k_{0y}=0}} \equiv \frac{1}{\tau(E_{0z})} \tag{29}$$

and carried out the dk_{0x} and dk_{0y} integrations in (25). By doing so, the incident electrons are essentially z-directed.

$$\vec{k}_0 = \hat{z}\, k_{0z} \quad . \tag{30}$$

Thus, for the transmitted electron we have

$$\vec{k}_1 = \hat{z}\, k_{1z} \tag{31}$$

and

$$\frac{\hbar^2}{2m_a^*} k_{0z}^2 + \Delta E_c = \frac{\hbar^2}{2m_b^*} k_{1z}^2 \tag{32}$$

The average ionization rate $\langle\frac{1}{\tau}\rangle$ is obtained by integrating Eq. (25) using Eq. (26). An upper bound of $\langle\frac{1}{\tau}\rangle$, $\langle\frac{1}{\tau}\rangle_u$, is obtained using the upper bound of $\frac{1}{\tau(E_0)}$. Dropping the subscript z and using E_0 instead of E_{0z}, one obtains for the integrand of Eq. (25)

$$\frac{1}{\tau(E_0)u} \equiv \frac{e^4}{\epsilon^2}\frac{4\pi}{\hbar^2}\left(\frac{L_{zn}}{L}\right)^2 \int \frac{d\vec{k}_{2t}}{(2\pi)^2 L_{zn}} f(\vec{k}_{2t})\,[S_u(\vec{k}_1,\vec{k}_{2n}^{+}) + S_u(\vec{k}_1,\vec{k}_{2n}^{-})]\ . \tag{33}$$

Below we first discuss the exact numerical integrations of $\frac{1}{\tau(E_0)}$ and $\langle\frac{1}{\tau}\rangle$ in Eq. (26) and Eq. (25). Then formulas for upper bounds, $\frac{1}{\tau(E_0)u}$, which lead to analytical expressions for $\langle\frac{1}{\tau}\rangle_u$ are presented.

3. THE NUMERICAL INTEGRATIONS

3.1. Integrations $\frac{1}{\tau(E_0)}$ and $\langle\frac{1}{\tau}\rangle$ from Eq. (26) and Eq. (25)

To obtain $\frac{1}{\tau(E_0)}$, we need to evaluate the electron-electron interaction integrals $S(\vec{k}_1,\vec{k}_{2n}^{\pm})$ in Eq. (12). For the following discussion, we use $\vec{k}_2 \equiv \vec{k}_{2n}^{+}$. The integral $S(\vec{k}_1,\vec{k}_2^{-})$ is obtained similarly, replacing $\vec{k}_{2n}^{+}$ by $\vec{k}_{2n}^{-}$, or $\frac{n\pi}{L_{zn}}$ by $\frac{-n\pi}{L_{zn}}$. For a parabolic band structure, and using

$$\vec{k}_1' = \vec{k}_{1t}' + \hat{z}k_{1z}' \tag{34}$$

$$\vec{k}_2' = \vec{k}_{2t}' + \hat{z}k_{2z}' , \tag{35}$$

the $\delta(E_1 + E_2 - E_1' - E_2')$ term in the integrand of (11) can be rewritten as

$$\frac{m_b^*}{\hbar^2}\,\delta[(k_{1z}' - k_{1z}'^{\alpha})(k_{1z}' - k_{1z}'^{\beta})] \tag{36}$$

where the two roots for k_{1z}', are

$$k_{1z}'^{\alpha} \equiv \frac{k_{1z} + \frac{n\pi}{L_{zn}}}{2} + \sqrt{\left(\frac{k_{1z} - \frac{n\pi}{L_{zn}}}{2}\right)^2 + \vec{k}_{1t}'\cdot\vec{k}_{2t} - k_{1t}'^2} \tag{37}$$

$$k_{1z}'^{\beta} \equiv \frac{k_{1z} + \frac{n\pi}{L_{zn}}}{2} - \sqrt{\left(\frac{k_{1z} - \frac{n\pi}{L_{zn}}}{2}\right)^2 + \vec{k}_{1t}'\cdot\vec{k}_{2t} - k_{1t}'^2} \tag{38}$$

Therefore, the k_{1z}' integration can be performed analytically using the properties of the delta functions, and k_{1z}' is restricted as given in Eq. (12). The other integrations can be simplified as

$$\int d\vec{k}_{2t} \int d\vec{k}'_{1t} = \int_0^{K_{2t}^{(n)}} k_{2t}\, dk_{2t} \int_0^{K'_{1t}} k'_{1t}\, dk'_{1t}\, 2\pi \int_0^{2\pi} d\phi_{12} \tag{39}$$

where the two angular variables ϕ_{2t} for $k_{2t}^{\vec{}\,'}$ and ϕ'_{1t} for $k_{1t}^{\vec{}\,'}$ have been transformed to only one angular variable ϕ_{12} which is the angle between $\vec{k}'_{1t}$ and $\vec{k}_{2t}$, with a 2π factor added as a result of this transformation because the integrand depends on ϕ_{12} only. The upper limit of k'_{1t} variable, K'_{1t}, is obtained from the condition that k'^{α}_{1z} and k'^{β}_{1z} in Eq. (37) and Eq. (38) should be real, i.e.,

$$\left(\frac{k_{1z} - \frac{n\pi}{L_{zn}}}{2}\right)^2 + k'_{1t}\, k_{2t} \cos\phi_{12} - k'^2_{1t} \geq 0 \quad . \tag{40}$$

This condition is easily included in the numerical code. If it is violated, k'^{α}_{1z} and k'^{β}_{1z} become imaginary and the integrand vanishes because the variable of integration, k'_{1z}, is real. Explicit solutions of Eq. (40) can also be used, which give the upper limit for k'_{1t},

$$K'^{+}_{1t} = \frac{k_{2t}}{2} + \sqrt{\left(\frac{k_{1z} - \frac{n\pi}{L_{zn}}}{2}\right)^2 + \left(\frac{k_{2t}}{2}\right)^2} \quad . \tag{41}$$

Then $\frac{1}{\tau(E_0)}$ can be written as:

$$\frac{1}{\tau(E_0)} = \frac{e^4 m_b^*}{\varepsilon^2 \hbar^3} \left(\frac{L_{zn}}{L}\right)^2 \frac{1}{4\pi^3 L_{zn}} \int_0^{K_{2t}^{(n)}} k_{2t}\, dk_{2t} \int_0^{2\pi} d\phi_{12}$$

$$\left\{\int_0^{K'^{+}_{1t}} k'_{1t}\, dk'_{1t} \int_0^{2\pi} d\phi_{12}\, F^{+}(k'_{1t}, k_{2t}, \phi_{12})\right.$$

$$\left. + \int_0^{K'^{-}_{1t}} k'_{1t}\, dk'_{1t} \int_0^{2\pi} d\phi_{12}\, F^{-}(k'_{1t}, k_{2t}, \phi_{12})\right\} \tag{42}$$

where

$$F^{+}(k'_{1t},k_{2t},\phi_{12}) \equiv \frac{1}{2\left\{\left[\frac{k_{1z}-\frac{n\pi}{L_{zn}}}{2}\right]^2 + k'_{1t}k_{2t}\cos\phi_{12} - k'^{2}_{1t}\right\}^{1/2}} \left\{\frac{1}{[k'^{2}_{1t} + (k_{1z} - k'^{\alpha}_{1z})^2 + q^2]^2} + \frac{1}{[k'^{2}_{1t} + (k_{1z} - k'^{\beta}_{1z})^2 + q^2]^2}\right\} \tag{43}$$

for k'^{α}_{1z} and k'^{β}_{1z} between k'_{th} and $k_{1z} + \frac{n\pi}{L_{zn}} - k'_{th}$, and zero for the appropriate terms otherwise. $F^{-}(k'_{1t},k_{2t},\phi_{12})$ and K'^{-}_{1t} are obtained by replacing $n\pi/L_{zn}$ by $-n\pi/L_{zn}$ in the F^{+} function as well as in K'^{+}_{1t} from Equations (41) and (43).

The last integration $\int dk_{0z}$ in $\langle\frac{1}{\tau}\rangle$ must be performed from a minimum $k^{\pm}_{0z,min}$ which is obtained from Eq. (12)

$$k_{1z} \geq 2k'_{th} \mp \frac{n\pi}{L_{zn}} \tag{44}$$

and the energy conservation relation Eq. (32),

$$k^{\pm}_{0z,min} = \sqrt{\frac{m^*_a}{m^*_b}\left(2k'_{th} \mp \frac{n\pi}{L_{zn}}\right)^2 - \frac{2m^*_a}{\hbar^2}\Delta E_c} \quad . \tag{45}$$

3.2. The Upper Bounds of the Integrals $\frac{1}{\tau(E_0)u}$ and $\langle\frac{1}{\tau}\rangle_u$ using Eq. (33) and Eq. (25)

The analytical result for the upper bound of $\frac{1}{\tau(E_0)}$ is

$$\frac{1}{\tau(E_0)u} = \frac{e^4 m^*_b}{\varepsilon^2\hbar^3}\left(\frac{L_{zn}}{L}\right)^2 \frac{1}{4\pi^2 q L_{zn}}[G^{+} + G^{-}] \equiv \frac{1}{\tau(E_0)}\Big|^{+}_{u} + \frac{1}{\tau(E_0)}\Big|^{-}_{u} \tag{46}$$

$$G^{\pm} = \sqrt{\left(\frac{K_{2t}}{q}\right)^2 + \left(\frac{k_{1z} \mp \frac{n\pi}{L_{zn}}}{q}\right)^2} - \left(\frac{k_{1z} \mp \frac{n\pi}{L_{zn}}}{q}\right)$$

$$- \tan^{-1}\sqrt{\left(\frac{K_{2t}}{q}\right)^2 + \left(\frac{k_{1z} \mp \frac{n\pi}{L_{zn}}}{q}\right)^2} + \tan^{-1}\left(\frac{k_{1z} \mp \frac{n\pi}{L_{zn}}}{q}\right) \quad . \tag{47}$$

Here the G^+ term is due to the term with $\vec{k}_{2n}^{++}$, and the G_2^- term due to that with $\vec{k}_{2n}^{+-}$ in Eq. (33), and

$$\left\langle \frac{1}{\tau} \right\rangle = \int_{k_{0z,min}^+}^{\infty} \frac{dk_{0z}}{2\pi} \left(\frac{\pi\hbar^2}{2m_a^* k_B T_e}\right)^{1/2} \exp\left(-\frac{\hbar^2 k_{0z}^2}{2m_a^* k_B T_e}\right) \frac{1}{\tau(E_0)}\Bigg|_u^+$$

$$+ \int_{k_{0z,min}^-}^{\infty} \frac{dk_{0z}}{2\pi} \left(\frac{\pi\hbar^2}{2m_a^* k_B T_e}\right)^{1/2} \exp\left(-\frac{\hbar^2 k_{0z}^2}{2m_a^* k_B T_e}\right) \frac{1}{\tau(E_{0z})}\Bigg|_u^- \tag{48}$$

which can be integrated numerically by Simpson's rule.

4. NUMERICAL RESULTS AND DISCUSSIONS

The direct numerical integrations of the ionization rate $\frac{1}{\tau(E_0)}$, and the average ionization rate $\langle\frac{1}{\tau}\rangle$ in Eq. (25) is straightforward. The upper bounds of the ionization rate and the exact numerically integrated results as functions of the energy of the incident hot electrons are shown in Figures 4(a) and 4(b). One can see that the ionization rate increases rapidly when the energy E_0 is above the threshold value E_i

$$E_i = \frac{\hbar^2}{2m_a^*} k_{0z,min}^{+2} = \frac{\hbar^2}{2m_b^*}\left(2k'_{th} - \frac{n\pi}{L_{zn}}\right)^2 - \Delta E_c \tag{49}$$

for each subband n = 1, 2, 3. The overall minimum threshold energy for impact ionization will be due to the highest occupied subband of course. For a quantum well size L_z = 200Å, Aℓ mole fraction x = 0.35 in the $A\ell_x Ga_{1-x}As$ region, and N_D = 5×10^{18} cm^{-3}, there are three occupied subbands among the six quantized levels in the well. The Fermi level is 0.1092 eV measured from the conduction band edge is the GaAs region. The threshold value for k'_{th}, (the minimum value of k'_{1z} or k'_{2z} for electrons 1' and 2' to get out of the quantum well) is given by

$$k'_{th} = \sqrt{2m_b^*(\Delta E_c - \delta)}\Big/\hbar \tag{50}$$

where δ accounts for the tilting of the quantum well due to the large applied field (Fig. 1). Without space charge effects we have

$$\delta \simeq eFL_z \tag{51}$$

where e is the magnitude of the electron charge. In all our computations we assume a field strength F = 10 kV/cm and a corresponding electron temperature of 2300° K at a lattice temperature of T = 77° K. (No accurate data for T_e in

$Al_xGa_{1-x}As$ are available to our knowledge. The above value is a result of Monte-Carlo simulations in GaAs. In reference 23 there are some discussions on F-T_e relations in $Al_xGa_{1-x}As$.) The necessary parameters used here are taken from references 24 and 25.

The average ionization rate $\langle\frac{1}{\tau}\rangle$ involves the integration over the energy E_0 and the distribution function. The upper bound of the impact ionization rate $\frac{1}{\tau(E_0)u}$ as a function of the energy E_0 is shown in Figure 4(a) for each subband and also for all subbands combined. These curves are much easier and faster to generate than the results of the exact numerical integration which are shown in Figure 4(b) since the results in Eq. (46) are analytical expressions. They also can serve as a means of checking the numerical accuracy of the exact numerical integral in Eq. (42). This is because $\frac{1}{\tau(E_0)u}$ from Eq. (46) is the upper bound of the numerical integral of $\frac{1}{\tau(E_0)}$ in Eq. (42). $\frac{1}{\tau(E_0)u}$ is the integration over over the whole spherical surface in Figure 3, for which all $\vec{k}_1'$ and $\vec{k}_2'$ of the two electrons are allowed everywhere on the spherical surface. $\frac{1}{\tau(E_0)}$ is the integration over only a portion of the spherical surface for which the condition $k_{th}' \leq k_{1z}' \leq k_{1z} + \frac{n\pi}{L_{zn}} - k_{th}'$ is satisfied. If one relaxes this condition in Eq. (43), the results of integration (42) will be over the whole spherical surface, which is the upper bound. Thus a numerical test in Eq. (42) by simply removing the constraints on k_{1z}' can be checked exactly with the analytical expression in Eq. (46). This process determines the number of discretized intervals for each integration variable in Eq. (42). One then adds the constraints on both k_{1z}' and k_{2z}' to obtain the exact numerical integrals.

4.1. The Effect of Multiple Subbands

As shown in Figures 4(a) and 4(b), the ionization rates due to higher level subbands are clearly very important because electrons in those subbands are in

higher energy levels and thus easier ionized. Figure 4(a) shows the upper bounds of the ionization rates for each subband and the total contribution is shown as the solid curve. The total rate in Figure 4(a) has a discontinuity whenever either a new subband with a term corresponding to either $+\frac{n\pi}{L_{zn}}$ or $-\frac{n\pi}{L_{zn}}$ term comes in. The results for the exact numerical integrations for $\frac{1}{\tau(E_0)}$ are shown in Figure 4(b) and the curves look smoother than those in Figure 4(a). (The small fluctuations in the curves of Figure 4(b) are due to numerical errors in the multiple integrations.) The electrons in the highest subband require the lowest threshold energy for impact ionization and there are more incident hot electrons with enough energy to impact ionize these electrons.

4.2. The Effect of the Quantum-Well Width L_z.

In Figures 5(a) and 5(b), we decrease L_z from 200Å to 80Å keeping the doping concentration N_D the same (5.0×10^{18} cm^{-3}). The upper bounds of the ionized rates are shown in Figure 5(a) and the exact numerical results are shown in Figure 5(b). There are three subbands for this structure and only the lowest one is occupied at this doping level. The ionization rate is smaller than the previous case in Figure 4(b). Roughly speaking, it is because the number of electrons per unit area in the quantum well region, $N_D L_z$, is smaller when L_z is decreased and N_D kept the same. Although the ground level of a thinner quantum well is higher than that of a thicker well in Figure 4(b), the higher subbands in Figure 4(b) also contribute to the total ionization rate and thus the ionization rate in the case in Figure 4(b) is larger.

4.3. The Effect of the Band Edge Discontinuity.

In Figures 6(a) and 6(b), we show the upper bounds of the ionization rates for all subbands and the results of the numerical integrations by decreasing the

Aℓ mole fraction x from 0.35 to 0.25 with L_z the same as that in Figures 4(a) and 4(b). We use the 60% - 40% rule[26,27] for the conduction and valence band edge discontinuities in our calculation. If one uses a different rule with a number between 60% to 85% for the conduction band edge discontinuity, the ionization rate will decrease because the well is deeper. Once ΔE_c is determined, the threshold energy for impact ionization can be obtained. Decreasing x will decrease ΔE_c, thus the threshold energy is lowered and the impact ionization rate is increased. This is clearly shown in Figures 6(a) and 6(b) as compared to Figures 4(a) and 4(b).

4.4. The Effect of Doping and the Total Ionization Rate.

If one increases the doping concentration in the quantum wells, one expects that the ionization rate will increase because there are more electrons available for impace ionization. This is shown in Figure 7 where the dashed line is for the upper bound of the ionization rate and the solid line is from exact numerically integration. Increasing N_D will increase the number of occupied subbands also since the Fermi level will be raised higher. For each N_D, the computation takes about 1500 cpu seconds as an average in the Cyber 175 Computer using about 1.6×10^6 number of dicretized points (40 for variable k_{2t}, 40 for k'_{1t}, 20 for ϕ_{12} and 50 for k_{0z}). When the Fermi level is raised, there will be more electrons in the higher subbands also and they are easier to be ionized since the minimum threshold energy is decreased. The other effect is that a higher doping concentration may also increase the tunneling probability of the bound electrons. This may also enhance the ionization rate.

5. POTENTIAL FOR DEVICE APPLICATIONS

Avalanche photodiodes which in their operational characteristic come close to the ideal of the conventional photomultiplier have been proposed by Capasso[2-6] and have been termed solid state photomultipliers. The principle of these devices is based on a highly asymmetric ionization coefficient for electrons (α) and holes (β). A conventional photomultiplier does, of course, not involve any holes at all. The question arises therefore if the new technological possibilities which are offered by MOCVD and MBE crystal growth techniques can be used to construct the complete solid state analogy of a photomultiplier. This question was one of the driving forces of our calculation in the previous sections. Instead of photomultiplier electrodes one would use quantum wells and the secondary electrons would be emitted into the neighboring AlGaAs instead of into vacuum. The results for the ionization rate in Figures 4-7 show indeed that appreciable gain can be achieved if the doping of the quantum well is $\sim 10^{19}$ cm^{-3} and the number of layers is larger than ~100. From Figure 7, the average ionization rate varies from 10^7 to 10^{10} 1/sec. Thus the electron ionization coefficients may vary from around 1 to 10^3/cm or higher assuming the average electron velocity is 10^7cm/sec or lower. The ionization rate can also be increased by decreasing the band edge discontinuity. Primary electrons can be generated by the absorption of infrared radiation either by the electrons in the valance band (interband absorption as shown in Figure 1) or by the quantum well electrons which make a transition from bound to propagating states. The latter type of free carrier absorption is of first order (the quantum well provides the momentum and phonons are not necessary) and therefore significantly stronger than the free carrier absorption in bulk semiconductors. This fact has been noted by Chiu et al.[28] who also show that multi-quantum well structures (similar to our

structure in Figure 1, except that they also dope the GaAℓAs regions) can be used as infrared detectors[7]. Chiu et al. did not, however, investigate the possibility of gain by the avalanche process. But, the possibility of varying the band-edge discontinuity (and therefore the range of infrared detection almost at will in the range of energies $0 \leq h\omega \lesssim 0.4$ ev) and the possibility of gain (analogous to the conventional photomultiplier) are enormously attractive features.

There are, however, also enormous technological problems which need to be overcome to realize such a device. Since holes are not involved, the electrons which are ionized out of the well need to be replenished. This means that separate ohmic contacts have to be applied to a number of sets of quantum wells without changing the high resistivity of the AℓGaAs layers in between. It may be possible to accomplish this complicated task with selective Schottky barrier contacts which would be ohmic for the highly doped quantum wells. Another severe problem is the require ment of highly doped quantum-wells neighboring to essentially depleted and highly resistive AℓGaAs. Both problems are not basic in nature and do not seem out of reach considering the recent progress in microstructure technology. However, more studies (including also the effects of field ionization) are needed to confirm and show the device potential of such structures.

Independently Capasso has recently performed experiments and has obtained encouraging evidence for impact ionization of the kind discussed in this paper. These experiments may call for an extension of our theory to include effects such as the tunneling-supported impact ionization[29,30] due to the band bending as shown in Figure 1. The bound electrons in the quantum well may acquire a

small amount of energy by collision with an incident hot electron and subsequently tunnel into the conduction band in the AℓGaAs region. This process reduces the ionization threshold energy in each subband. Thus the ionization rates as for example shown in Figure 4(b) may start from a lower threshold value for each subband and may also be enhanced because of the tunnel-impact ionization process. More work needs to be done to predict the precise performance of such a structure.

6. CONCLUSIONS

The impact ionization across the conduction band-edge discontinuity of quantum-well heterostructures has been studied. A geometrical configuration to illustrate the contribution to the electron-electron interaction in the momentum space has been shown. The average ionization rate has also been calculated for various doping concentrations and geometries. We have included the contributions from the multi-subbands and the nonparabolicity effects in our calculations. The application of this impact ionization mechanism to a solid state superlattice photomultiplier has also been discussed.

ACKNOWLEDGEMENTS

The discussions with J. P. Leburton, J. J. Coleman, and T. Wang are appreciated. This research is supported by the NASA grant NAG 1-500 and the Joint Services Electronics Program.

APPENDIX A
THE SCREENING PARAMETER q

The dielectric screening parameter in the static limit is given by [31]

$$q = \left[\frac{e^2}{\varepsilon} \int g(E) \left(-\frac{\partial f^0}{\partial E}\right) dE\right]^{1/2} \tag{A1}$$

which is the Thomas-Fermi screening parameter, and it reduces to 1/(Debye length) for a Maxwellian-Boltzmann distribution in the case of a nondengenerate electron gas.

When the electron concentration is degenerate, and the temperature is low, we obtain the Thomas-Fermi screening parameter using a three-dimensional density of states.

$$q = \left(\frac{m^* e^2}{e\hbar^2}\right)^{1/2} \left[\frac{3n}{\pi 4}\right]^{1/6} \tag{A2}$$

where n is the electron concentration.

If we consider a two-dimensional density of state $g_{2D}(E)$, we can carry out the integral in (A1) since $g_{2D}(E)$ is a constant and obtain

$$q = \left(\frac{m^* e^2}{\varepsilon\hbar^2}\right)^{1/2} \left(\frac{N}{\pi L_z}\right)^{1/2} \tag{A3}$$

where N is the number of occupied subbands. Our calculations for a quantum well of size L_z = 200 Å and $\Delta E_c \cong 0.3$ eV show that Eq. (A2) and (A3) give almost the same result for a large n.

APPENDIX B

THE QUANTIZED ENERGY LEVELS E_{Qn} IN A QUANTUM WELL INCLUDING THE EFFECTIVE MASS DIFFERENCE

The energy level E_{Qn} are obtained by using the boundary conditions

$$\psi_a = \psi_b \tag{B1}$$

$$\frac{1}{m_a^*}\frac{\partial \psi_a}{\partial z} = \frac{1}{m_b^*}\frac{\partial \psi_b}{\partial z} \tag{B2}$$

at the two interfaces $z = 0$ and $z = L_z$. The result is the well-known eigenequation:

$$\tan kL_z = \frac{2\alpha}{1 - \alpha^2} \tag{B3}$$

where

$$k = (2m_b^* E)^{1/2}/\hbar \tag{B4}$$

$$\alpha = \left(\frac{m_b^*}{m_a^*} \frac{\Delta E_c - E}{E} \right)^{1/2} \tag{B5}$$

The eigenequation (B3) includes both the even and odd solutions for the wave functions. The number of quantized levels in the quantum well is easily determined from the criterion:

$$\text{If} \quad \frac{(N-1)\pi}{2} < \frac{(2m_b^* \Delta E_c)^{1/2} L_z}{2\hbar} < \frac{N\pi}{2} \quad , \tag{B6}$$

the number of quantized levels = N.

APPENDIX C

AVERAGE EFFECT MASS m_b^* IN GaAs REGION (REGION b) WITH THE NONPARABOLICITY EFFECT INCLUDED

The E-k relation including the nonparabolic effect is

$$E\,(1 + \alpha E) = \frac{\hbar^2 k^2}{2m^*} \tag{C1}$$

where we use $\alpha = 0.67\ (eV)^{-1}$, $m^* = 0.063\ m_0$ at 77° K, and m_0 is the electron mass in free space.

Using the definition

$$\frac{1}{m^*_{eff}(E)} = \frac{1}{\hbar^2}\frac{\partial^2}{\partial k^2} E \tag{C2}$$

and

$$m_b^* = \frac{\int_0^{\Delta E_c} m^*_{eff}(E)\,dE}{\Delta E_c} \tag{C3}$$

where ΔE_c is the conduction band edge discontinuity, we obtain analytically

$$m_b^* = m^*\,(1 + \alpha\Delta E_c)\,(1 + 2\alpha\Delta E_c + 2\alpha^2\Delta E_c^2) \tag{C4}$$

The above procedure accounts for the nonparabolic effect up to the energy ΔE_c. We then use this average value m_b^* in the parabolic band structure for GaAs in our calculation for the ionization rates.

REFERENCES

1. R. Chin, N. Holonyak, Jr., G. E. Stillman, J. Y. Tang and K. Hess, Electron. Lett., 16, 467 (1980).

2. F. Capasso, W. T. Tsang, A. L. Hutchinson, and G. F. Williams, Appl. Phys. Lett. 40, 38 (1982).

3. F. Capasso and W. T. Tsang, International Electron Devices Meeting, Technical Digest, 334, 1982.

4. F. Capasso, IEEE Trans. Nucl. Sci., NS-30, 424 (1983).

5. F. Capasso, W. T. Tsang and G. F. Williams, IEEE Trans. Electron Devices, ED-30, 381 (1983).

6. F. Capasso, J. Vac. Sci. Technol. B, 1, 454 (1983).

7. J. S. Smith, L. C. Chiu, S. Margalit, and A. Yariv, J. Vac. Sci. Technol. B, 1, 376 (1983).

8. F. Capasso, S. Luryi, W. T. Tsang, C. G. Bethea, and B. F. Levine, Phys. Rev. Lett., 51, 2318 (1983).

9. G. C. Osbourn, J. Vac. Sci. Technol. B, 2, 176 (1984).

10. D. R. Myers, J. J. Wiczer, T. E. Zipperian, and R. M. Biefeld, IEEE Electron Device Letters, EDL-5, 326 (1984).

11. Y. Horikoshi, A. Fischer, and K. Ploog, Appl. Phys. Lett. 45, 919 (1984).

12. G. H. Dohler, Superlattices and Microstructures, 1, 279 (1985).

13. P. T. Landsberg and A. R. Beattie, J. Phys. Chem. Solids, 8, 73 (1959).

14. A. R. Beattie and P. T. Landsberg, Proc. Roy. Soc. A249, 16 (1959).

15. P. T. Landsberg, C. Phys-Roberts and P. Lal, Proc. Phys. Soc., 84, 915 (1964).

16. P. T. Landsberg, Phys. Stat. Solids 41, 457 (1970).

17. M. Takeshima, J. Appl. Phys., 43, 4114 (1972).

18. C. Smith, R. A. Abram, and M. G. Burt, Superlattices and Microstructures, 1, 119 (1985).

19. A. Sugimura, IEEE J. Quantum Electron., EQ-19, 932 (1983).

20. J. M. Ziman, Electrons and Phonons, Oxford University Press, Amen House, London, 1960.

21. A. Matulionis, J. Pozela and A. Reklaitis, Solid State Commun., 16, 1133 (1975).

22. K. Huang, Statistical Mechanics, John Wiley & Sons, Inc., New York, 1963, 59-60.

23. S. Adachi, J. Appl. Phys., 58(3), R1 (1985).

24. H. C. Casey, Jr., and M. B. Panish, Heterostructure Lasers, Part A: Fundamental Principals, Academic Press, Inc., 1978.

25. J. S. Blakemore, J. Appl. Phys., 53, R123 (1982).

26. R. C. Miller, A. C. Gossard, D. A. Kleinman, and O. Munteanu, Phys. Rev. B, 29, 3740 (1984).

27. R. C. Miller, D. A. Kleinman, and A. C. Gossard, Phys. Rev. B, 29, 7085 (1984).

28. L. C. Chiu, J. S. Smith, S. Margalit and A. Yariv, Appl. Phys. Lett. 45, 331 (1983).

29. A. S. Kyuregyan, Sov. Phys.-Semicond., 10,410 (1976).

30. F. Capasso, Physics of Avalanche Photodiodes in Semiconductors and Semimetals, Vol. 22, Part D, Chapter 1, Eds., R. K. Willardson and A. C. Beer, Academic Press, Inc., New York, 1985.

31. J. M. Ziman, Principles of the Theory of Solids, Second Edition, Section 5.2, Cambridge University Press, Cambridge, 1972.

FIGURE CAPTIONS

Figure 1. Geometry of a structure exhibiting impact ionization across the band-edge discontinuity of quantum-wells.

Figure 2. The initial and final states for the electron-electron interaction in a quantum well structure.

Figure 3. A geometrical configuration in $\vec{k}$-space to illustrate the electron-electron interaction integral. With both the energy and the momentum conserved, the four electron wave vectors are on the same spherical surface. The integrations over $k_1^{\vec{}\,'}$ and $k_2^{\vec{}\,'}$ are restricted to the shaded portion with the z-component between k'_{th} and $k_{1z} + \frac{n\pi}{L_{zn}} - k'_{th}$, (n=1).

Figure 4(a). The upper bound of the impact ionization rates $\frac{1}{\tau(E_0)_u}$ as functions of the incident hot electron energy E_0 ($\equiv E_{0z}$) for each subband and the sum of all three subbands. The parameters used are L_z = 200Å, L = 1200Å, $N_D = 5 \times 10^{18} cm^{-3}$, x = 0.35, T = 77°K, T_e = 2300°K ($m_a^* = 0.09m_0$, $m_b^* = 0.105m_0$, ΔE_c = 0.262 eV).

Figure 4(b). The exact impact ionization rates from numerical integration of Eq. (25) and (42). The same material parameters as those in 4(a) are used here.

Figure 5(a). The upper bound of the impact ionization rate as a function of the incident hot electron energy E_0 for a different quantum well width L_z = 80 Å. (L = 1200Å, x = 0.35, $N_D = 5 \times 10^{18} cm^{-3}$, $m_a^* = 0.09m_0$, $m_b^* = 0.105m_0$, ΔE_c = 0.262 eV). There is only one occupied subband at this doping level.

Figure 5(b). The exact impact ionization rate as a function of the incident hot electron energy E_0 obtained from numerical integration of Eq. (25) using Eq. (42). The same parameters as those in Figure 5(a) are used here.

Figure 6(a). The upper bound of the impact ionization rates as functions of the incident electron energy E_0 for a smaller Barrier height ($x = 0.25$, $\Delta E_c = 0.187$ eV) than that in Figure 4. We use $m_a^* = 0.105\ m_0$, $m_b^* = 0.083\ m_0$ for this value of x and ΔE_c. The other parameters are $L_z = 200$Å, $L = 1200$Å, $N_D = 5 \times 10^{18} cm^{-3}$.

Figure 6(b). The impact ionization rates as functions of the incident electron energy E_0. Same parameters are used as in Figure 6(a).

Figure 7. The average ionization rate $\langle \frac{1}{\tau} \rangle$ (solid curve) and its upper bound $\langle \frac{1}{\tau} \rangle_u$ (dashed curve) as functions of the doping concentration N_D in in the quantum well. We use $L_z = 200$ Å, $L = 1200$ Å, $x = 0.25$, $T = 77°$ K, $T_e = 2300°$ K. The parameters m_a^*, m_b^* and ΔE_c are the same as in Fig. 6(a).

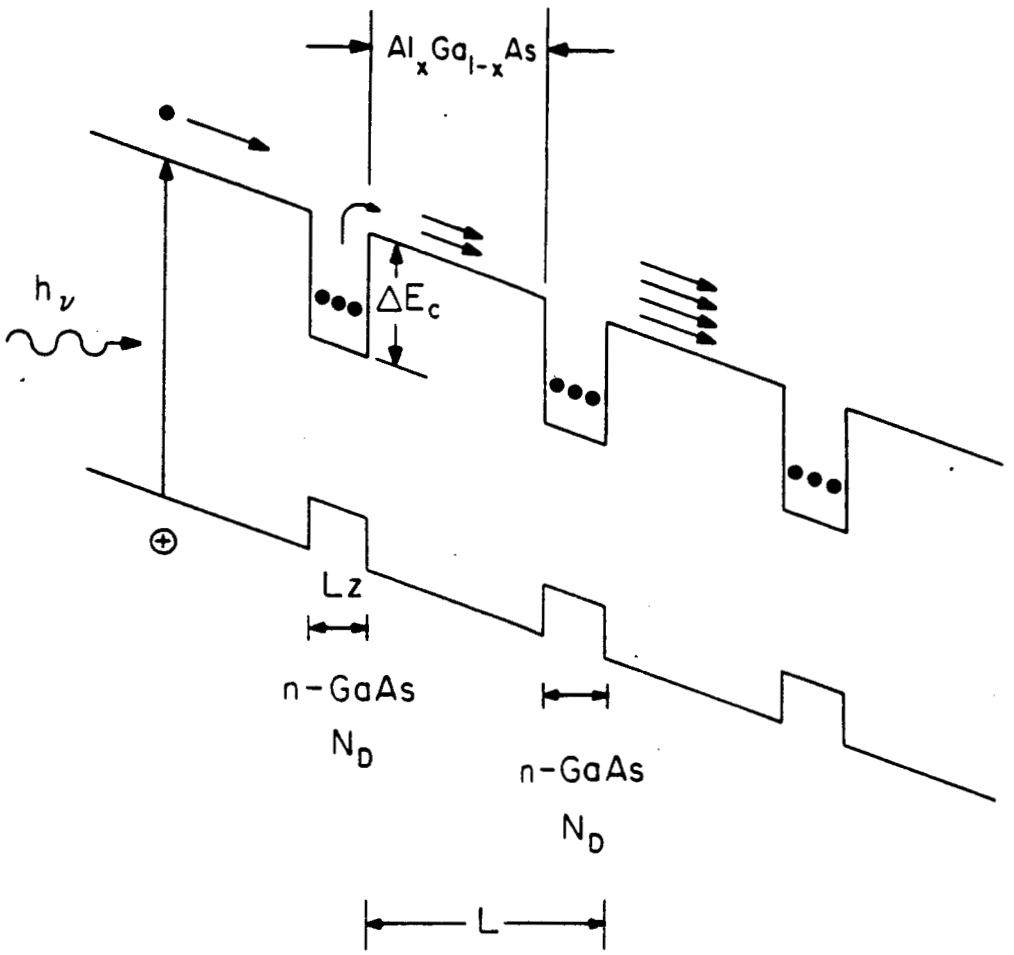

Figure 1

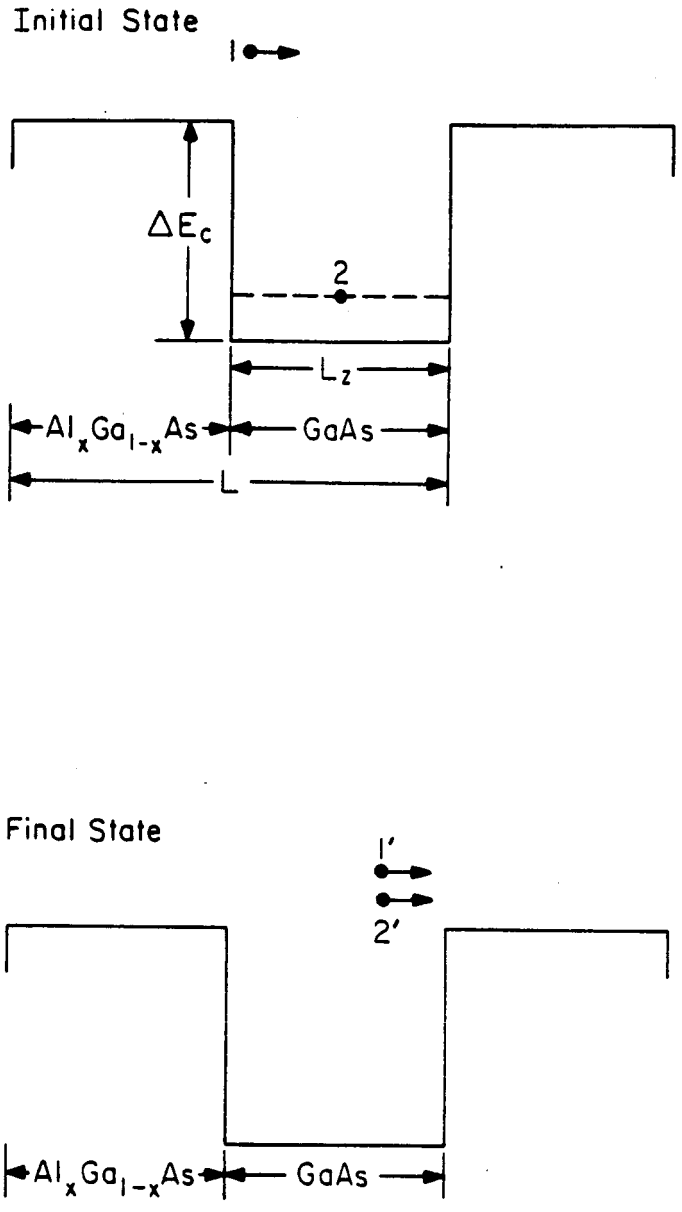
Initial State
1
ΔEc
2
Lz
AlxGa1-xAs
GaAs
L
Final State
1'
2'
AlxGa1-xAs
GaAs

Figure 2

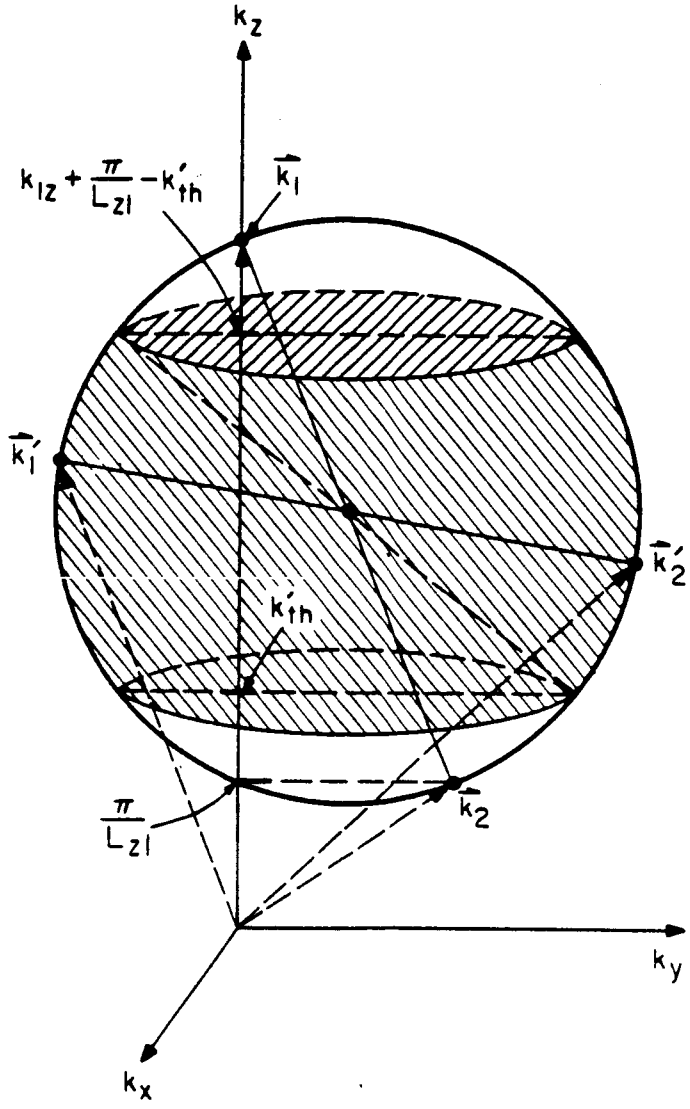
k_z
$k_{1z} + \frac{\pi}{L_{z1}} - k'_{th}$
$\vec{k}_1$
$\vec{k}'_1$
$\vec{k}'_2$
k'_{th}
$\frac{\pi}{L_{z1}}$
$\vec{k}_2$
k_y
k_x

Figure 3

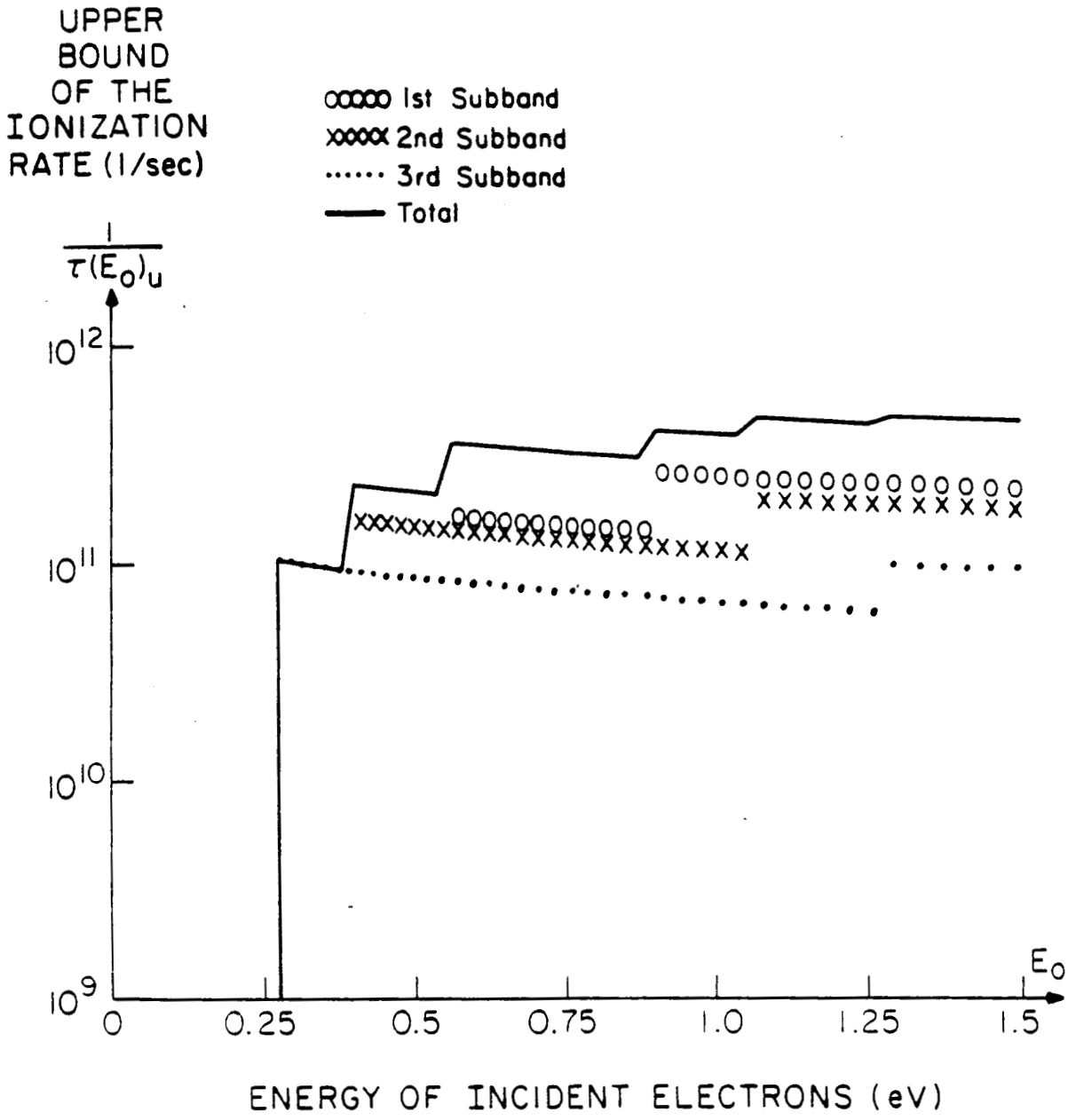
UPPER BOUND OF THE IONIZATION RATE (1/sec)
1st Subband
2nd Subband
3rd Subband
Total
$\frac{1}{\tau(E_0)_u}$
10^{12}
10^{11}
10^{10}
10^{9}
0
0.25
0.5
0.75
1.0
1.25
1.5
E_0
ENERGY OF INCIDENT ELECTRONS (eV)

Figure 4(a)

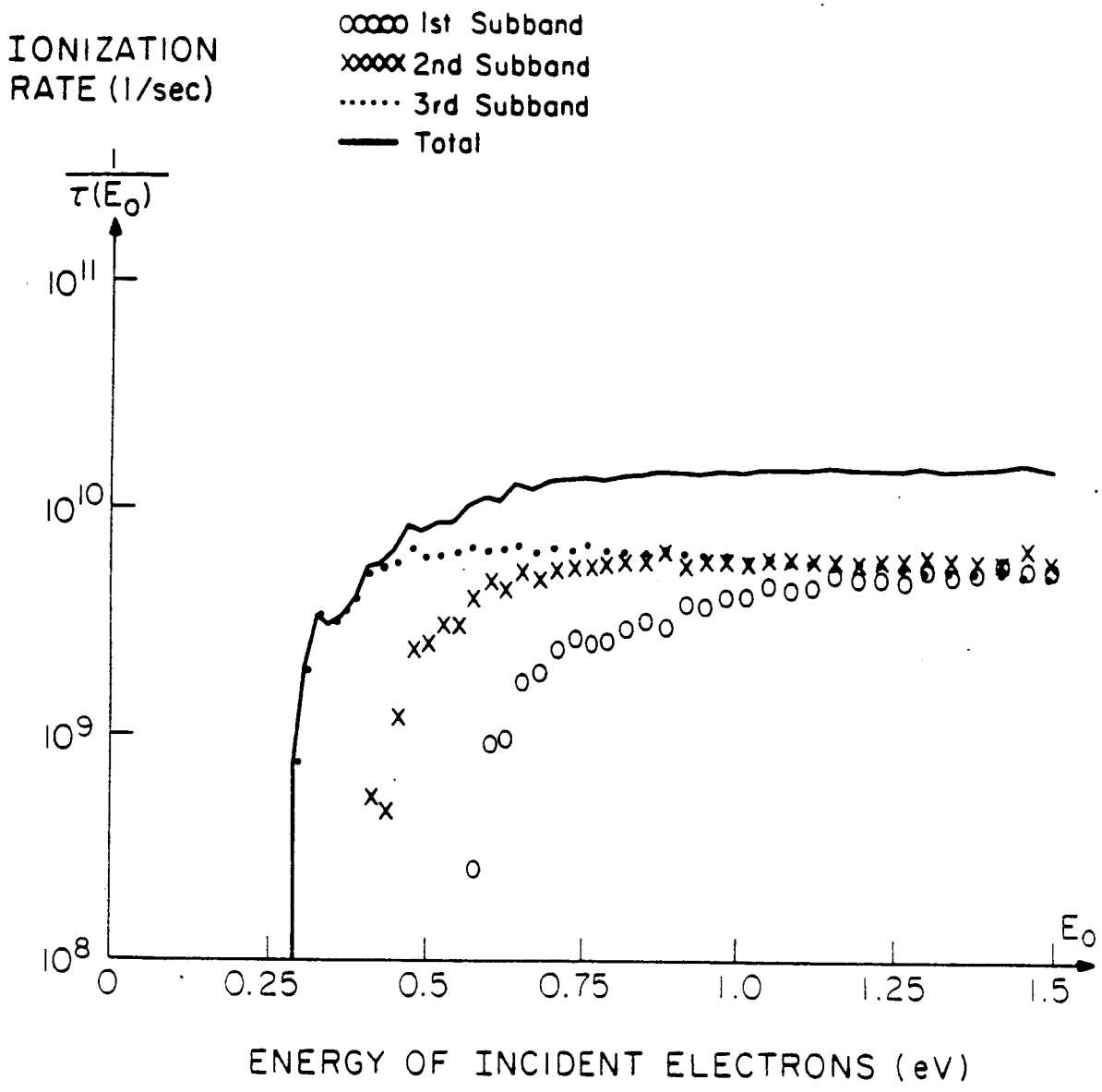
IONIZATION
RATE (1/sec)
1st Subband
2nd Subband
3rd Subband
Total
$\frac{1}{\tau(E_o)}$
10^{11}
10^{10}
10^{9}
10^{8}
0
0.25
0.5
0.75
1.0
1.25
1.5
E_o
ENERGY OF INCIDENT ELECTRONS (eV)

Figure 4(b)

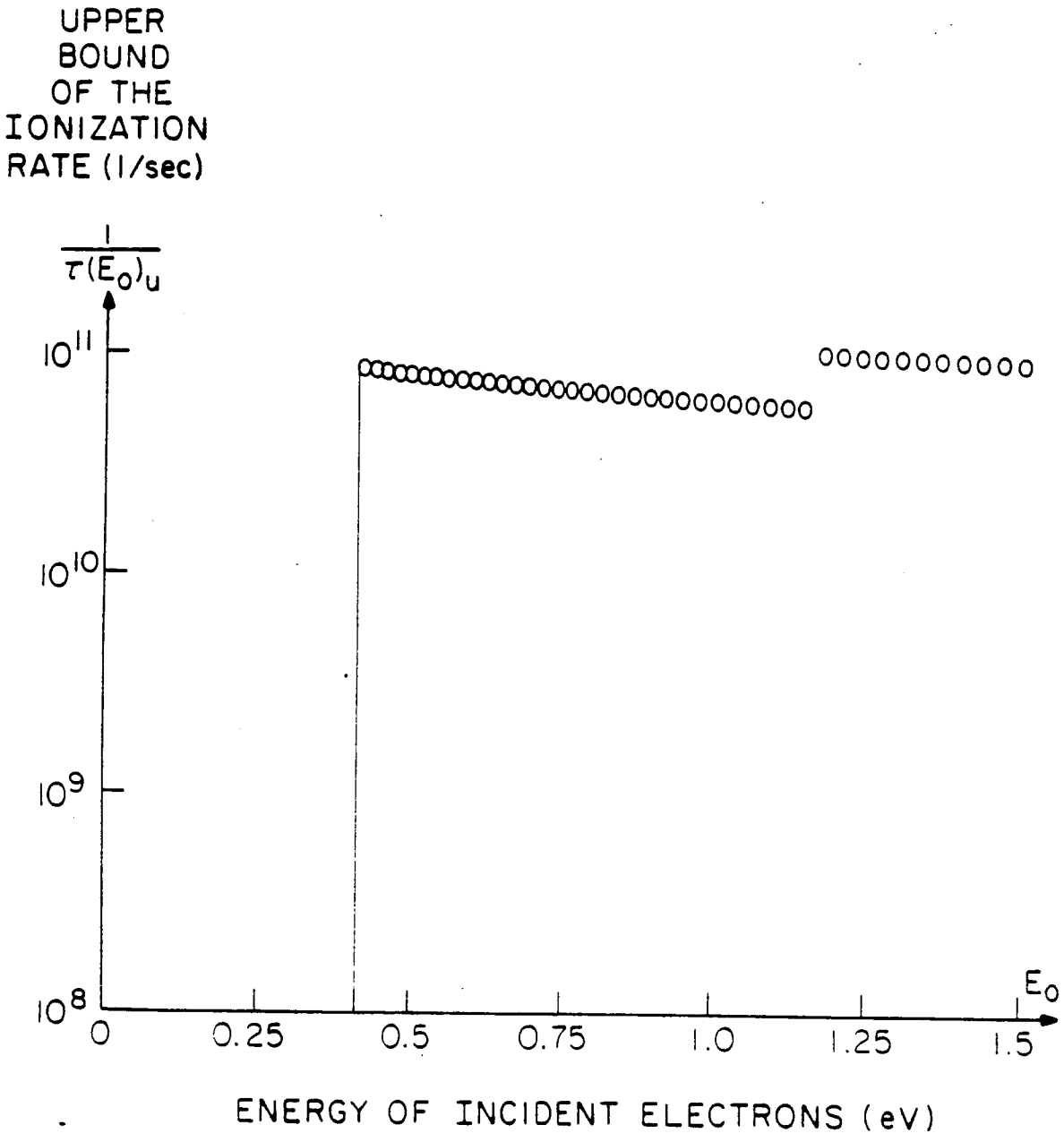
UPPER
BOUND
OF THE
IONIZATION
RATE (1/sec)
$\frac{1}{\tau(E_0)_u}$
10^{11}
10^{10}
10^{9}
10^{8}
0
0.25
0.5
0.75
1.0
1.25
1.5
E_0
ENERGY OF INCIDENT ELECTRONS (eV)

Figure 5(a)

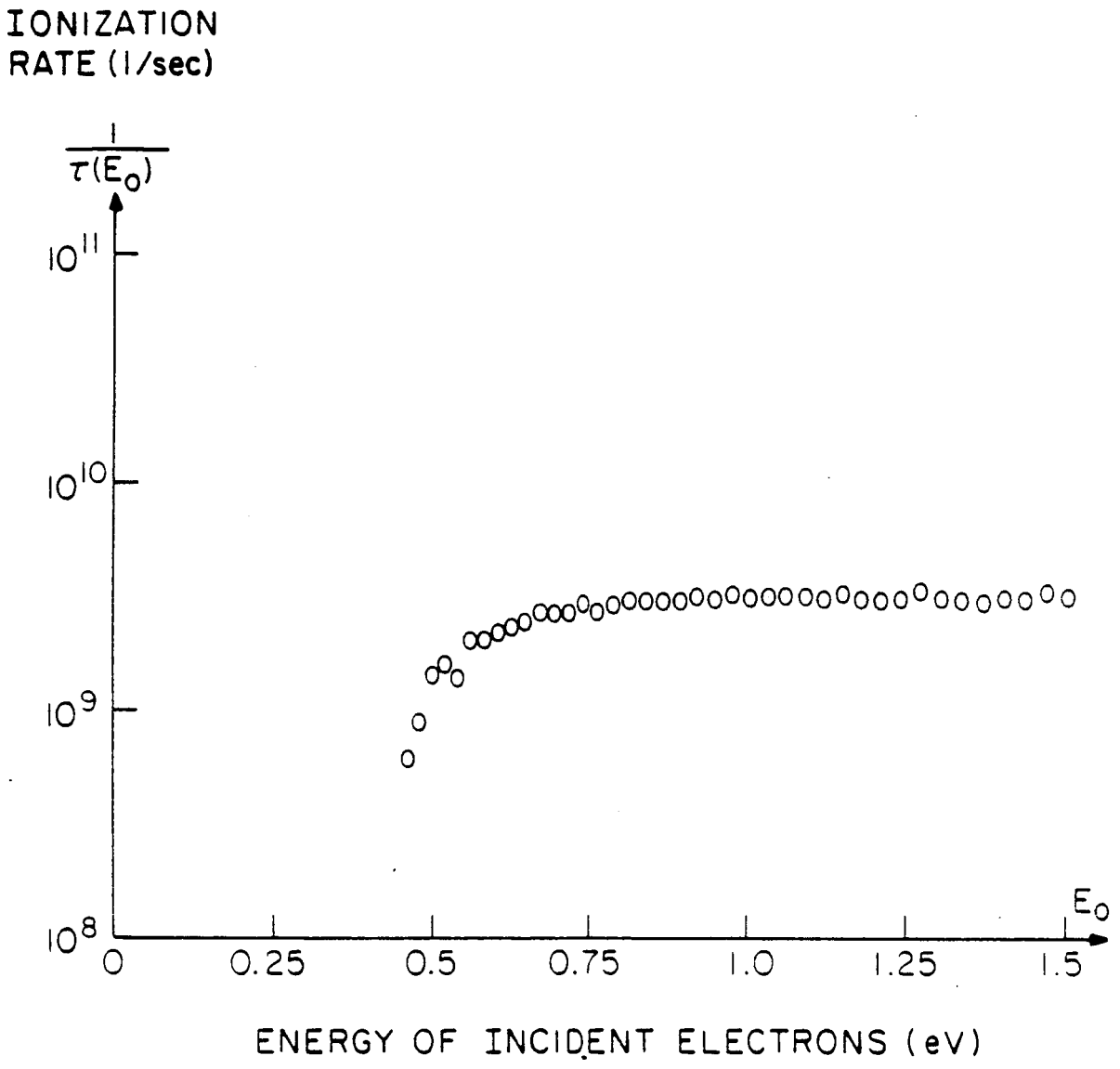
IONIZATION
RATE (1/sec)
1/τ(E0)
10^11
10^10
10^9
10^8
0
0.25
0.5
0.75
1.0
1.25
1.5
E0
ENERGY OF INCIDENT ELECTRONS (eV)

Figure 5(b)

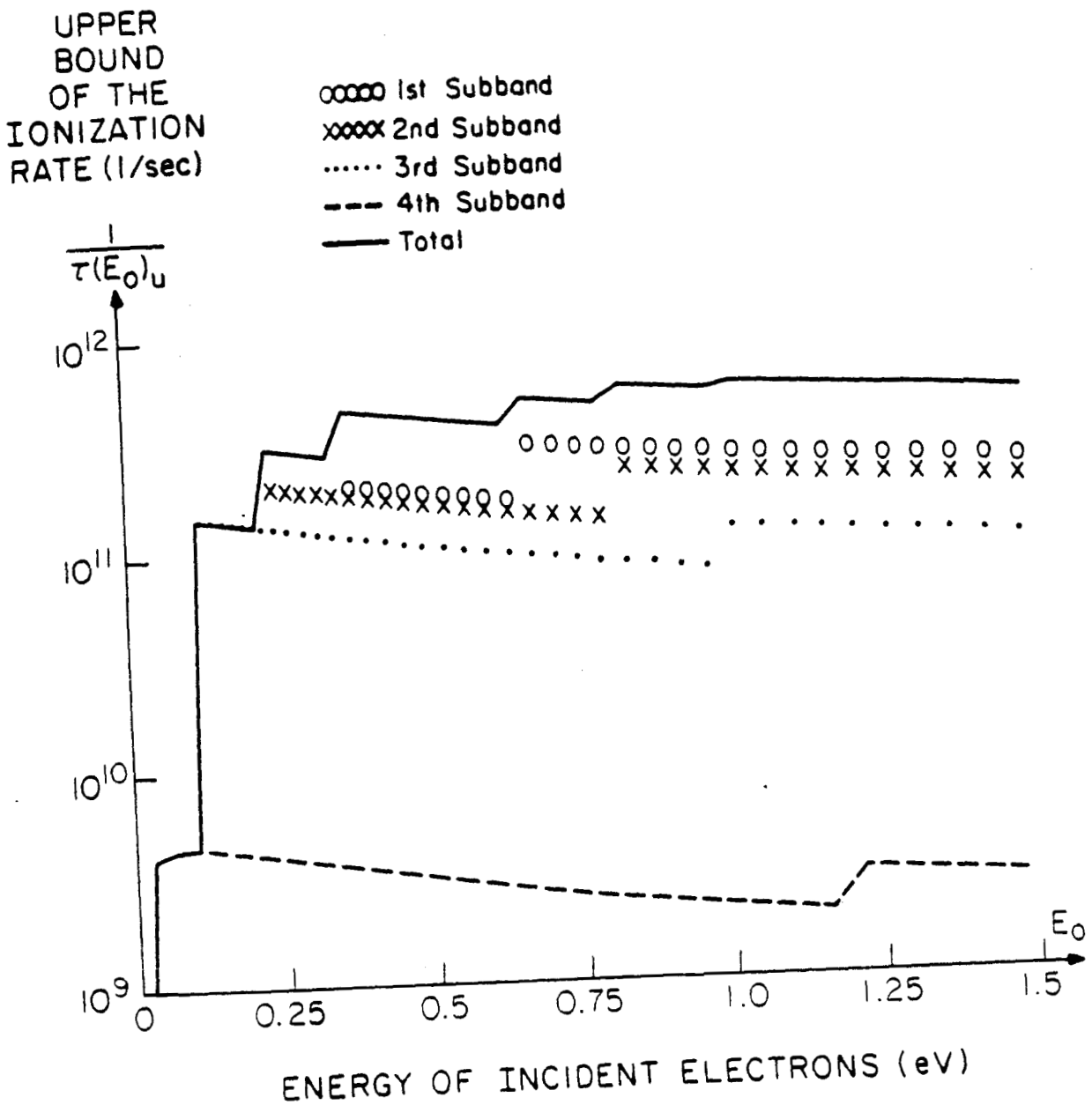
UPPER BOUND OF THE IONIZATION RATE (1/sec)
1st Subband
2nd Subband
3rd Subband
4th Subband
Total
$\frac{1}{\tau(E_0)_u}$
10^{12}
10^{11}
10^{10}
10^{9}
0
0.25
0.5
0.75
1.0
1.25
1.5
E_0
ENERGY OF INCIDENT ELECTRONS (eV)

Figure 6(a)

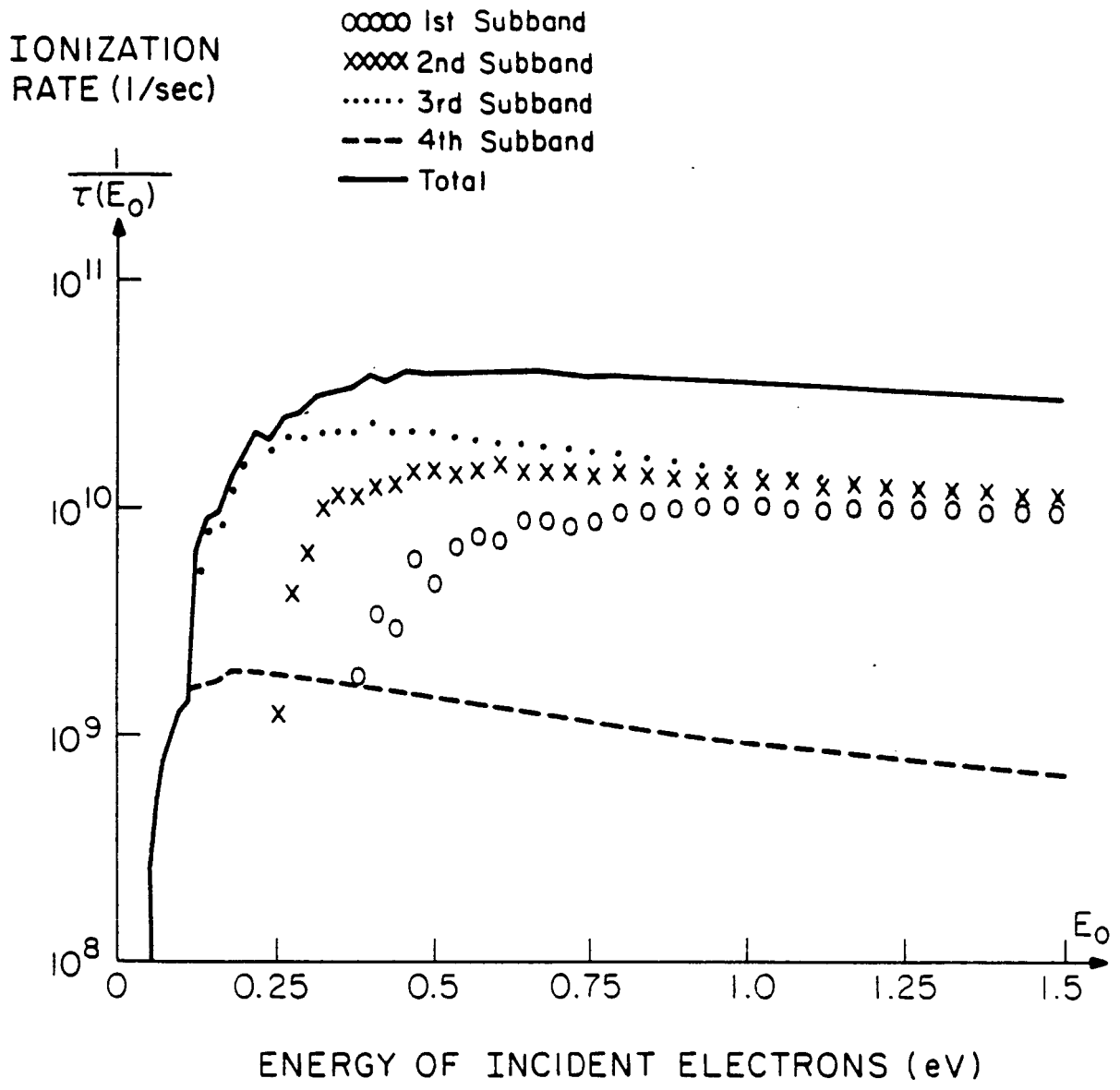
IONIZATION
RATE (1/sec)
1st Subband
2nd Subband
3rd Subband
4th Subband
Total
$\frac{1}{\tau(E_0)}$
10^{11}
10^{10}
10^{9}
10^{8}
0
0.25
0.5
0.75
1.0
1.25
1.5
E_0
ENERGY OF INCIDENT ELECTRONS (eV)

Figure 6(b)

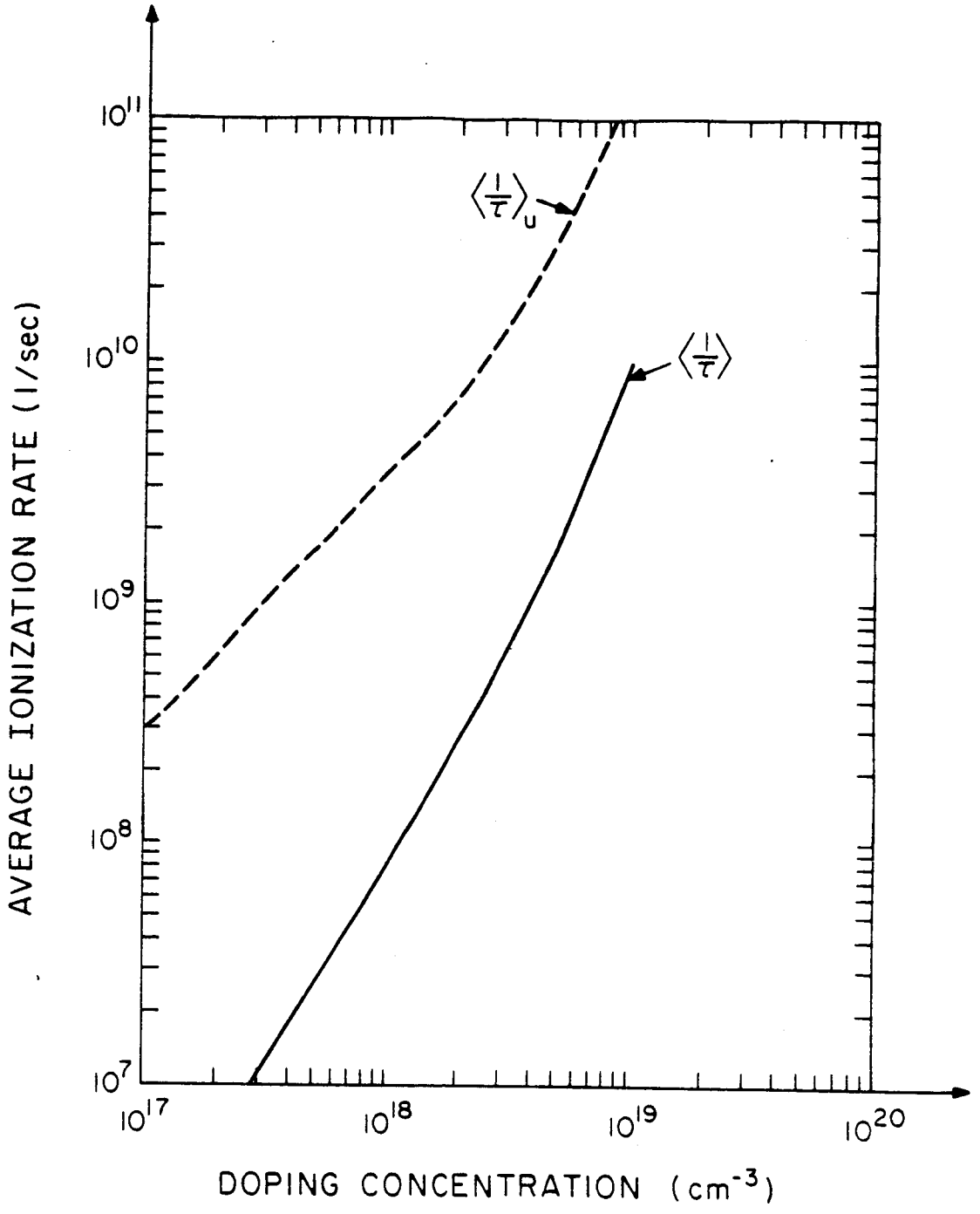
AVERAGE IONIZATION RATE (1/sec)
10^{11}
10^{10}
10^{9}
10^{8}
10^{7}
$\langle \frac{1}{\tau} \rangle_u$
$\langle \frac{1}{\tau} \rangle$
10^{17}
10^{18}
10^{19}
10^{20}
DOPING CONCENTRATION (cm^{-3})

Figure 7